JOURNAL OF PROPULSION AND POWER
Vol. 25, No. 3, May–June 2009

Experimental Investigations of Pressure Distortions on the High-Pressure Compressor Operating Behavior

Niko Reuß* and Christian Mundt†
University of the Bundeswehr Munich, 85577 Neubiberg, Germany

DOI: 10.2514/1.37412

Experimental investigations of coupled total pressure inlet distortion effects on the unsteady behavior of the five-stage high-pressure compressor Rig 212 from the RB199-jet engine development have been carried out in this work. The total pressure inlet distortions were generated by two distortion generators in the intake, facilitating the combination of steady and unsteady distortion. The determination of the flowfield in the compressor inlet plane immediately in front of the first rotor showed a very complex pattern with abrupt changes in the distribution of pressures, angles, and Mach numbers. An explicit allocation of generated distortions was possible. Evidence was obtained of an interaction between distortions, even in undistorted sectors. The expected strong loss of power was seen in the compressor map similar to a suction-side throttling, meaning an inlet flow reduction with a lowering of the surge margin toward lower pressure ratios. No dependency was determined between the rotation direction of distortion and the location of the surge margin. The flow analysis in the compressor inlet plane and through the machine in the axial direction showed merely slight differences at the beginning of stall in all configurations with distortion. The type of distortion has, however, an influence on the fully developed stall. There were no indications of prestall effects when the distortion generators were used.

Nomenclature

C = compressor, configuration
n = speed

I. Introduction

IN A jet engine, the function of the compressor is to compress the working medium air. Thermal efficiency and, consequently, the specific fuel consumption (SFC) are affected. Because SFC plays a major role in the direct operation costs (DOC) of an aircraft, great effort is required in the development phase of a jet engine to optimize the efficiency.

The flow through a compressor necessitates an increasing pressure. For this reason, there is always the danger of boundary-layer separation. Thus, the analysis of aerodynamic instabilities in compressors is a matter of particular interest. Several numerical studies have been published. However, because the focus of this work is experimental, these will not be reviewed here.

In a two-spool jet engine, the compression process is conducted by a low-pressure compressor (LPC) and a high-pressure compressor (HPC). The HPC has a higher aerodynamic load, which is why the HPC is more vulnerable to aerodynamic instabilities such as rotating stall and surge. Extreme flight maneuvers may result in flow separation at the intake. This is represented by steady total pressure inlet distortions. These might pass the through the LPC and enter the HPC [1]. Furthermore, it is possible that a LPC develops rotating stall, generating rotating total pressure inlet distortions in the HPC. A combined occurrence of both phenomenon may result in an increased mechanical load on the engine. Inlet distortions corrupt the flowfield in the compressor inlet plane; this can lead to aerodynamic instabilities. It is important to ascertain the circumstances which may lead to this critical behavior.

Received 5 March 2008; revision received 26 September 2008; accepted for publication 7 November 2008.

*Doctor of Engineering, Institute for Jet Propulsion, Werner-Heisenberg-Weg 39; currently MAN Turbo Corporation; niko.reuss@gmx.de.

†Professor, Doctor of Engineering, Institute for Thermodynamics, Werner-Heisenberg-Weg 39; christian.mundt@unibw.de.

Longley [2] analyzed rotating total pressure inlet distortion effects on the behavior of a four-stage HPC. He used a distortion generator which could rotate in the same and the opposite directions to the compressor rotor at up to 100% spool speed. The most important results are the influence of the rotating speed and direction of the distortion generator disk. When the distortion was rotating in the same direction as the compressor rotor, the decrease of the surge margin was stronger than for the counter-rotating configuration. Thus, the location of the surge margin is a function of speed and direction of the rotating inlet distortions.

Throttling of a compressor beyond the surge line generates unsteady operating behavior. One branch of research deals with the detection of such instabilities and subsequent active stabilization of the compressor (Scheidler et al. [3] or Buhr et al. [4], for example). In these studies, however, the development of the flow was studied without intervention. Depending on the compressor speed and size of the plenum on the pressure side, this unsteady behavior may include rotating stall or surge. In the experimental apparatus, rotating stall was observed in the compressor (Rig212) with the small plenum between the compressor exit and the first throttle device for all speed lines, whereas compressor surge was initiated when using the throttle downstream of the air receiver [5].

This work describes the flow analysis after crossing the stability line. This analysis refers to wall pressure transducer measurements which are set up circumferentially at the compressor intake and arranged axially at the 0 deg position within the annulus between the stages. The aim is to investigate the effects of inlet distortions on the compressor operating behavior during stall, as well as the development of flow instabilities. In addition, the characteristics of fully developed distortion are compared with an undistorted reference.

Although literature exists regarding the interaction of compressors with steady or rotating distortion (Moore [6] or Longley [2] for example), there are to date very few investigations of coupled total pressure inlet distortion on the behavior of a compressor.

II. Experimental Setup

A. Compressor Rig

The compressor used is the five-stage HPC Rig212 formerly used in the European Turbo Union RB199 jet engine development program (see Fig. 1). The Rig212 was analyzed with regard to aerodynamic stability for insertion as the HPC in the RB199.

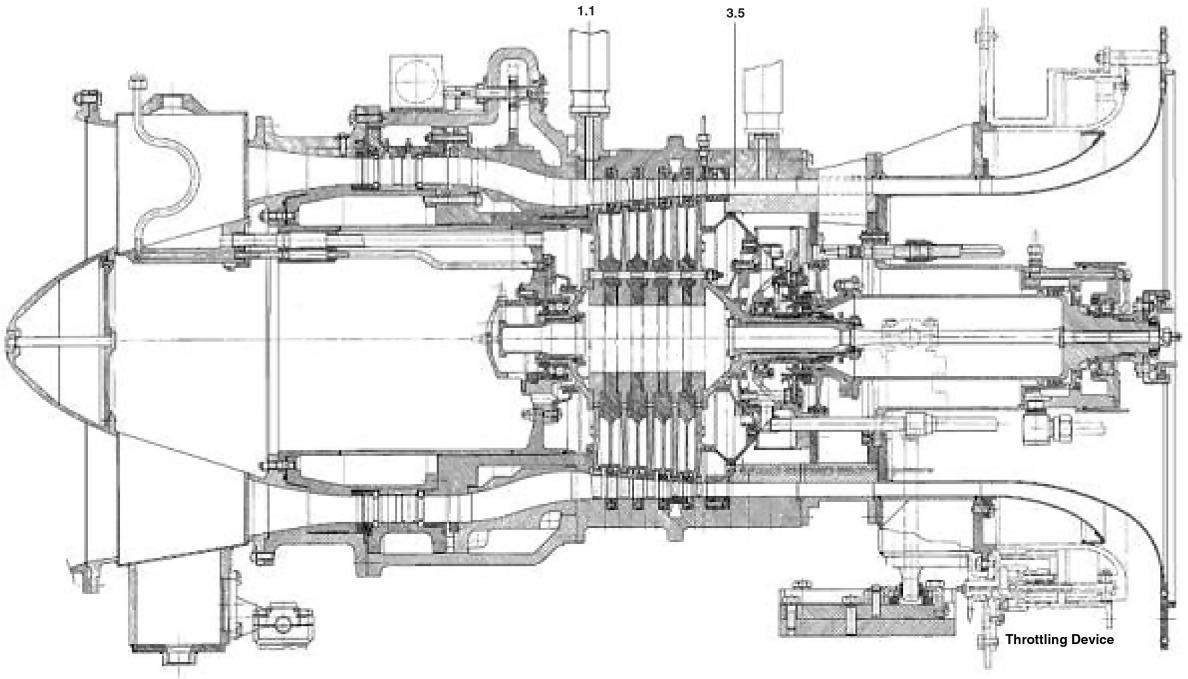

Fig. 1 Compressor Rig212.

Previous use of the compressor before commencing the research at the Institute of Air Propulsion in 1995 dates back to 1975. The compressor design, however, is still representative of the HPC found in current aircraft engines. The compressor is divided into four main components. These include the 1) intake casing with transition channel, 2) compressor casing with stator, 3) compressor spool with rotor, and 4) outlet casing.

Under International Standard Atmosphere test conditions, the compressor provides a pressure ratio of 2.87 at a mass flow of 4.68 kg/s and 13,860 rpm design speed. A bleed behind the third stage reduces the mass flow by 3%. The hub-to-tip ratio varies from 0.84 to 0.9. At the design point condition, the relative inlet Mach number of the first rotor is 0.86 at the mean radius, which is 168.6 mm.

B. Engine Test Facility

Driven by a 1 MW dc motor, the Rig212 is installed in an open-circuit test facility. In a filter house, the incoming air is filtered down to a particle size lower than 5 μm. The filtered atmospheric air is then accelerated through a mass flow measurement nozzle. The sensors for defining the mass flow are located at the smallest cross section of the nozzle. For the compressor map and the location of the operating point, it is very important that these sensors function accurately. Using total pressure probes to traverse the flowfield enables a measurement of the boundary-layer thickness and yields a flow coefficient. This coefficient facilitates an exact calculation of the air mass flow.

The mass flow measurement nozzle supplies the following settling chamber with air. Because of the large diameter, the air is decelerated. In the settling chamber, there are three perforated metal plates which homogenize the incoming air. Temperature sensors are located on the third plate, which is the closest to the compressor. The obtained temperature data can be used for the compressor inlet because the flow from the settling chamber to the compressor can be considered as adiabatic when no rotating inlet distortion is generated. A cone-shaped passage connects the settling chamber with the compressor and reduces the cross section to the diameter of the compressor inlet plane.

Downstream of the compressor, the air flow is controlled by a throttle device. The small exit plenum prevents the occurrence of surge if the compressor stalls. The bleed air from the third stage is mixed with the compressor air in the following chamber. This chamber is terminated by another throttle device to control the axial compressor. The use of this device leads to compressor surge. Finally, the air passes an exhaust silencer before being released back into the atmosphere.

C. Inlet Distortion Generators

To generate the total pressure distortions in the compressor inlet flow, the distortion generators are located in the compressor intake. Two distortion generators are installed: a steady-state and a rotating total pressure distortion generator. They can be operated separately or simultaneously.

1. Steady-State Distortion Generator

The S-shaped compressor intake simulates the transition from the intermediate pressure compressor (IPC) to the HPC in the RB199 jet engine. The adapter for the steady-state distortion generator (SDG) is located in this section. The SDG is a distortion screen with bars of rectangular profile. The bars are positioned in a 60 deg sector on the circumference to generate a sectorized steady-state total pressure loss.

The SDG can be pivoted around the annulus by a step motor. Thus, it is possible to traverse the complete flowfield even with the stationary probes that can only be traversed from hub to tip at a single position in the annulus.

2. Rotating Distortion Generator

The rotating distortion generator (RDG) simulates rotating stall from the LPC (or IPC) in a twin-spool (or triple-spool) jet engine with rotating total pressure inlet distortions. The generation of distortions occurs in a similar manner to that in the SDG. The disk of the RDG is a single unit with bars of rectangular profile. The bars are positioned in a 120 deg sector on the circumference to generate a sectorized rotating total pressure loss. The RDG is driven by a 19 kW ac motor, the maximum speed of which is limited to 9000 rpm, that is, 65% of the compressor design speed. The rotating inlet distortion can be generated co- and counter-rotating with respect to the compressor rotor. The free choice of speed and direction of the RDG is an advantage compared to an actual twin-spool jet engine.

The experimental setup facilitates an insight into a realistic twin-spool jet engine configuration with both compressors rotating in the same direction to reduce the circumferential velocities in the shaft

bearings. For an actual jet engine, the LPC/HPC rotor speed ratio is around 50–70%. The speed of the rotating stall in the LPC section is approximately 40–50% of the LPC rotor speed around the annulus [7]. The RDG is capable of reproducing inlet distortion at these speeds.

The compressor design allows the positioning of a rotating device upstream of the whole rig. Mixing processes between the distorted and undistorted area are to be expected. A high flow speed is required in the distortion generator disk plane to generate a total pressure distortion. Therefore, the compressor intake had to be modified by reducing the casing radius and providing slight acceleration through the entire compressor inlet duct. To avoid aerodynamically induced flutter of the distortion generator bars, the compressor shaft speed is limited to 93.3% of the design speed.

While the RDG is in use, thermal energy is added to the flow. For this reason, the flow from the settling chamber to the compressor is no longer adiabatic. With increasing RDG speed and compressor spool speed, the power required for the RDG rises. Taking into account a motor mechanical efficiency of 95%, the entire power is transformed into thermal energy. The resulting maximum temperature rise is about 2.5K at the maximum compressor spool speed.

3. *Generation of Distortion*

Both distortion generators generate the inlet total pressure losses in the same way. They have a screen of sharp-edged bars with a rectangular profile. If the Reynolds number is within a range of $10^2 < Re < 10^4$, the flow conditions are similar. The operating range of the compressor is within the specified range of Reynolds number. For the determination of the total pressure loss, Roach [8] established the following equation:

$$\frac{\Delta p_t}{q} = A\left(\frac{1}{\beta^2} - 1\right)^B \quad \text{with} \quad \beta = 1 - \frac{d}{M} \tag{1}$$

The coefficients A and B remain constant due to the similar flow conditions. They were calculated to $A = 0.98$ and $B = 1.09$ for both distortion generators. The thickness of the bars is defined by d, and M defines the distance between two bars. The screen porosities are calculated to $\beta_{\mathrm{SDG}} = 0.6935$ and $\beta_{\mathrm{RDG}} = 0.5079$.

According to the equation the loss and thus the intensity of distortion is solely dependent on the dynamic pressures q_{SDG} and q_{RDG}. It is now possible to define the design total pressure loss in terms of the compressor spool speed. However, the equation does not consider the flow in the undistorted sector. Thus the actual total pressure loss will be less than that calculated. Furthermore, possible interaction between the generators is not considered.

D. Data Acquisition

The instrumentation of the Rig212 and the compressor test facility can be divided into a low- and a high-frequency section according to the frequency response of the sensors. Both are coupled to a peripheral component interconnect bus system. The steady-state data acquisition triggers the unsteady-state data acquisition. This has the advantage of very accurate synchronization.

1. *Steady State*

The steady-state data acquisition system measures 64 channels simultaneously at a fixed sampling rate of 1000 Hz (subsequently time averaged to 100 Hz) per sensor on a 32 bit resolution A/D converter.

The low-frequency instrumentation consists of the pressure and temperature sensors for the calculation of mass flow, pressure ratios, and other global data. In addition, the rotor shaft speed is also measured.

The data acquisition system allows the online monitoring of the compressor, yielding information regarding selected measurement channels as well as stored operating points in the compressor map. The reference map is used to approximate the current configuration.

2. *Unsteady State*

High-frequency data acquisition allows measurement of 16 channels with a sampling rate of 100 kHz per sensor on a 32 bit resolution A/D converter. This frequency spectrum is sufficient to resolve the unsteady character of the combined steady-state and rotating inlet total pressure distortions and even the flow fluctuations during the stall inception process. The signals are automatically filtered below the Nyquist frequency to avoid aliasing effects. Nevertheless, the detection of the blade passage frequencies of all stages is possible.

Kulite pressure transducers (XCS/XCE–062 SG) represent the high-frequency instrumentation: a wall pressure sensor array with six equally spaced sensors around the annulus is located in the compressor inlet and used for the analysis of the stall inception process. Furthermore, a sensor is located between each stage. For the measurement of the flowfield in the compressor inlet plane, unsteady-state pneumatic three-hole probes are used. In each probe, three Kulite pressure transducers are installed. Determination of the flow angle and Mach number is possible via the pressure signals. It is even possible to calculate flow velocities using cross correlations. The probes are located on three fixed circumferential positions and can be traversed from hub to tip. The possibility of rotating the SDG and RDG enables measurement of the entire flowfield. Because of the high hub-to-tip ratio, the two-dimensional measurements are acceptable. A detailed description of the experimental setup including the data acquisition is provided by Reuß [5].

E. Configurations

The main focus of the work is the analysis of the compressor operating behavior under various inlet flow conditions. This is realized by the variation of the distortion generator configurations. The combination of SDG and RDG (co- and counter-rotating) enables six possible configurations for all compressor speed lines. Figure 2 shows configurations 5 and 6 (C5, C6) with the distortion generators (RDG left, SDG right), the casing, the hub, and the ribs.

Reference configuration 1 (C1) is without distortion generators. Configurations 5 and 6 include the combined application of both generators. In C5, the RDG is corotating and, in C6, counter-rotating. Only one distortion generator is installed in the remaining configurations (C2-SDG, C3-RDG corotating, C4-RDG counter-rotating).

III. Inlet Flowfield

The analysis of the coupled total inlet pressure distortions concerns the development of distortion along the intake from the position of generation to the compressor inlet plane immediately preceding the first rotor. It is of importance to investigate the presence of possible interaction between distortions.

Downstream of the distortion generators, mixing processes occur at the edges of the distorted flow sector. Because of the static pressure gradient, air flows from the undistorted to the distorted sector. If a rotor blade enters this area, the flow is directed toward the blade. From an aerodynamic point of view, the blade loading is reduced. When the rotor blade exits the distorted sector, the angle of incidence

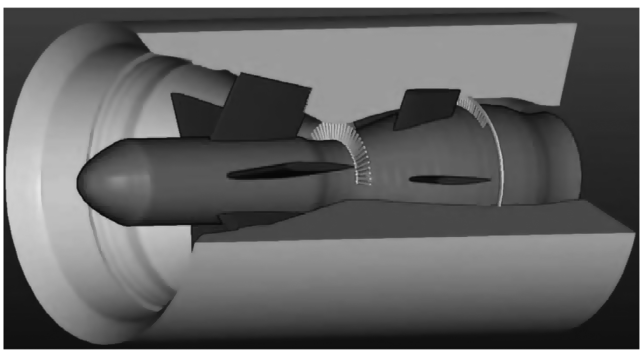

Fig. 2 Configurations 5 and 6 (RDG left, SDG right).

increases. The aerodynamic loading on the blade increases as a result. The smaller this region, the shorter the occurrence of higher aerodynamic load and the influence on the rotor blade flow is reduced. In other words, the efficiency of the inlet distortions is best and the performance of the rotor blade flow is worst when the intersection distortion period is at its longest. This can be achieved at low compressor speeds or, alternatively, by corotating total inlet pressure distortion as demonstrated by Longley [2] and Peters [9].

Rotating stall in the LPC section of a twin-spool jet engine subjects the HPC to a higher mechanical loading equivalent to that of approximately 20–40% of the HPC-rotor speed.

According to the preceding considerations, it is expected that the influence of the generated distortions should decrease at higher compressor spool and RDG speeds due to the shorter exposure period in the distorted flow sector. However, the intensity of distortion is mainly dependent on the dynamic pressure at the screens of the distortion generators. The dynamic pressure increases at high compressor spool speeds because of the higher mass flow.

The following results of the measurement of the flowfield in the compressor inlet plane at distorted conditions were determined using the multihole pressure probes and high-frequency data acquisition. The probes were positioned at 0 deg for probe 1 (P1) and 120 deg for probe 2 (P2) at the circumference. For the combined operation of the distortion generators (C5, C6), P1 was located directly in the center of the distorted sector of the SDG, whereas P2 was in the undistorted sector. The flowfield was measured at the following locations: near the hub, mean radius, and near the tip.

Figure 3 shows a relative total pressure loss ($\Delta p_{t,\mathrm{rel}} = [p_t - p_{t,\mathrm{ref}}]/p_{t,\mathrm{ref}}$) along the unwound circumference. The reference pressure is the total pressure either from C1 or the maximum pressure at the analyzed speed line. Because of the periodic character of the rotating inlet total pressure distortions from the RDG, the signals are ensemble averaged to minimize stochastic irregularities. This technique uses the length of one period calculated by a spectral analysis, and so generates a time-averaged period.

Total pressure, Mach number, and flow angle are determined using the measured probe pressures. The Mach number and flow angle distribution are illustrated via gray-scaled bars. The distribution of the total pressure loss was centered on the maximum loss. The Mach number and flow angle are offset in the diagram accordingly.

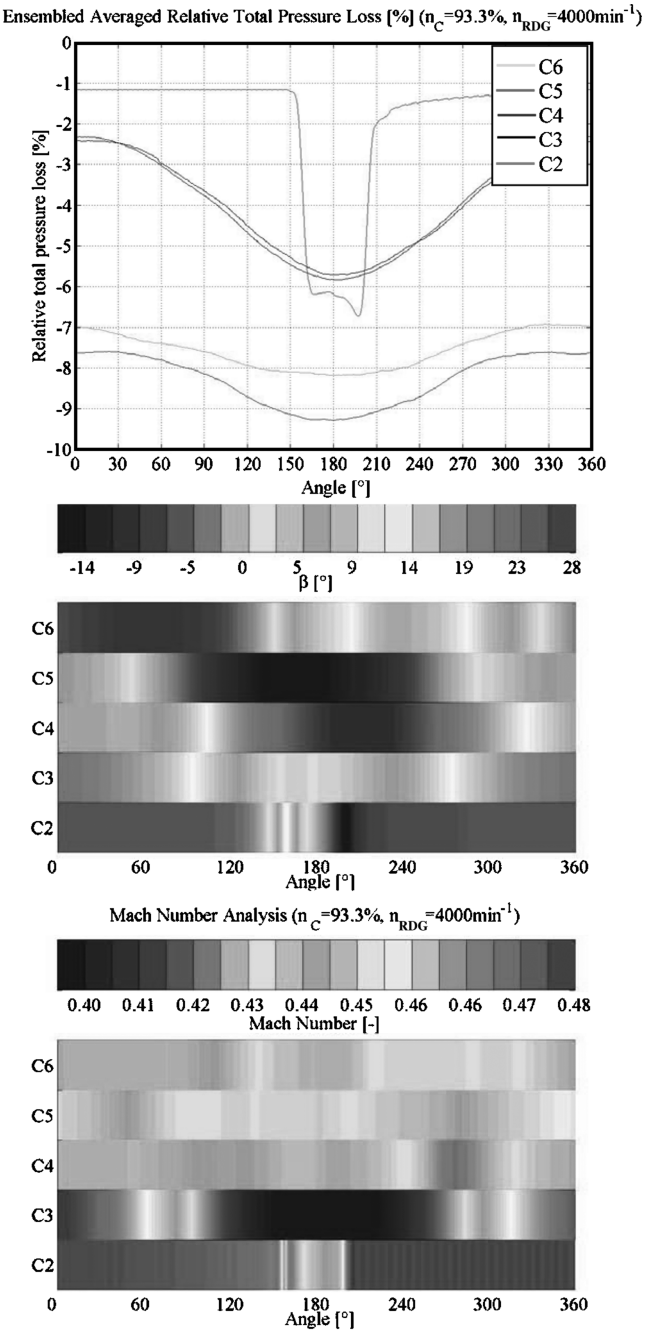

Fig. 3 Different total pressure inlet distortions (P1).

A. Comparison of Configurations with Regard to Compressor Speed

As expected, the strongest influence is caused by the different SDG and RDG configurations. The sole use of the SDG (C2) generates a 60 deg circumferential partial obstruction of the annulus. The sole use of the RDG (C3, C4) generates a higher total pressure loss with a distorted sector of 120 deg. The strongest distortion is reached using the SDG and RDG together in a coupled fashion (C5, C6) because a sector can be distorted by up to 180 deg. A matter of particular interest is the flowfield and compressor operating behavior for the separate use of the generators (C2, C3, C4) vs the combined use of the generators (C5, C6). The question arises as to whether or not the sum of the separate distortions (C2 + C3 and C2 + C4) causes the same integral and maximum total pressure loss as the combined sum.

Figure 3 shows the distribution of the relative total pressure loss. Mach number and flow angle in the compressor inlet plane are measured by P1 at the mean radius. All configurations are shown with reference to the 93.3% compressor speed line at a stable operating point near the surge line.

At C5 and C6, the SDG is fixed so that P1 is centered in the distorted sector while the speed of the RDG is adjusted to 4000 rpm. In the figure, the expression min^{-1} is used for rpm. The figure shows an ensemble-averaged rotation of the RDG and the distortion development through the SDG.

The maximum total pressure shows the various distortion intensities of each configuration clearly. The SDG generates a stronger maximum total pressure loss (6.7%) than the RDG (5.8%). This effect is caused by the RDG speed as shown next. The coupled operating configuration has the strongest influence (C5 = 9.3%, C6 = 8.2%).

An interesting result is that C5 with the corotating RDG generates a higher maximum total pressure loss than C6 with counter-rotating RDG. This seems to verify the aforementioned consideration that a long exposure period of the rotor blades in the distorted area has a greater effect on the compressor. C3 and C4, however, do not show these differences, but rather a symmetric distribution. C3, C4 and C5, C6 are arranged symmetrically. The compressor with its constant direction of rotation is the only asymmetric factor. Thus, an interaction between the SDG and the RDG is responsible for the illustrated flowfield.

Because of the special test arrangement the integral, total pressure loss is the sum of the ensemble-averaged loss generated by the RDG in one circulation and the relative total pressure loss of the SDG at the position of the probe. It can be observed that the integral losses of two comparable configurations, such as C3/C4 and C5/C6, are almost identical. The sum of the integral losses of C2 + C3 and C2 + C4 is larger than the integral losses of C5 or C6 and increases with

increasing compressor spool speed. The reason for this phenomenon is the special arrangement of the distortion generators. During combined operation (C5, C6), with SDG inside the distorted sector of the RDG, the flow enters the SDG with reduced axial velocity. This leads to the lower losses in combined operation vs the sum of separate distortions.

Because of the close proximity of the probes to the compressor, an upstream effect is measurable in order of a vortical flow in the direction of compressor rotation. At C2, the SDG is moved slowly into the annulus. Because of the stationary character of the distortion, the vortical flow at the edges of the distorted sector is compensated. However, in the undistorted sector, a negative flow angle remains which increases with increasing compressor spool speed ($-2\ \text{deg}/n_C$ at 70% to $-5\ \text{deg}/n_C$ at 73.3%). If the RDG is used, the averaged flow direction is dependent on the direction of rotation of the RDG. Because of the wake of the RDG, the static pressure gradients at the edges of the distorted sector cannot compensate. This wake moves in the same rotating direction as the RDG. Because of the rising flow velocity with increasing compressor spool speed, and therefore increasing static pressure gradients, an increase of angle maxima is observed. This effect is stronger at C6 than at C5. It suggests that the mixing of the flow is greater at C6. The total pressure distribution validates this assumption.

The steady-state total pressure distortion generated by the SDG reduces the Mach number in the distorted sector. The distribution of the Mach number is similar to the total pressure distribution and defines a clearly limited area. At the edges of the distorted sector, the flow is accelerated by the static pressure gradients. It is indicated by the rising Mach numbers in these areas. The Mach number distribution for configurations using the RDG is in contrast to this. Analogue to the flow angle distribution, the configurations with identical rotating direction of the RDG show similar Mach number distributions. At C3 and C5, the Mach number minimum is at the same position as the total pressure minimum. The Mach number minimum occurs at C4 and C6 just after the total pressure minimum.

Figure 4 shows the comparison between C5 and C6 at the 93.3% speed line on an operating point near the surge line measured by P2 at the 120 deg circumferential position. Thus, the probe is not located in the distorted sector of the SDG. The RDG rotates at $n_{\text{RDG}} = 4000$ rpm. The shape of the relative total pressure distribution is very similar in contrast to the shape behind the SDG. As C3 and C4 show, there is an almost symmetric pattern. But the total pressure amplitude of C6 is larger than that of C5. The maximum and the integral total pressure losses are approximately 1–1.5% higher than for the sole use of the RDG. The distributions of flow angle and Mach number are also similar to those of C3 and C4. Even at this position, the influence of the SDG on the flow is noticeable. The higher Mach number level vs C3 and C4 indicates an acceleration of the flow leaving the SDG.

Figure 5 shows the influence of the compressor spool speed on the relative total pressure loss measured by P1 at the steady-state working line. C5 is shown and C6 can be found in [5]. Besides the distorted sector size, the compressor spool speed is the variable with the second largest influence on the distortion intensity. Furthermore, the axial flow velocities with an open throttle device are higher than the velocities at operating points near the surge line.

When looking at the total pressure distribution, an increase of the relative total pressure loss can be identified for increasing compressor speed. With regard to the increase of the losses, a quadratic dependence of dynamic pressure on axial flow velocity at the distortion screens can be determined. With increasing compressor spool speeds, the shape of the distortion becomes more pronounced. That is, on one hand, the maximum total pressure losses increase and, on the other hand, the flow mixing decreases in proportion with the more defined shape of the distortion. Thus, the limits between distorted and undistorted sectors are defined more clearly.

To explain this issue, two superposed phenomena have to be considered. Indeed, with the increasing losses due to the increasing compressor spool speeds, the static pressure gradients are higher and cause a stronger mixing. However, at this point, another effect is

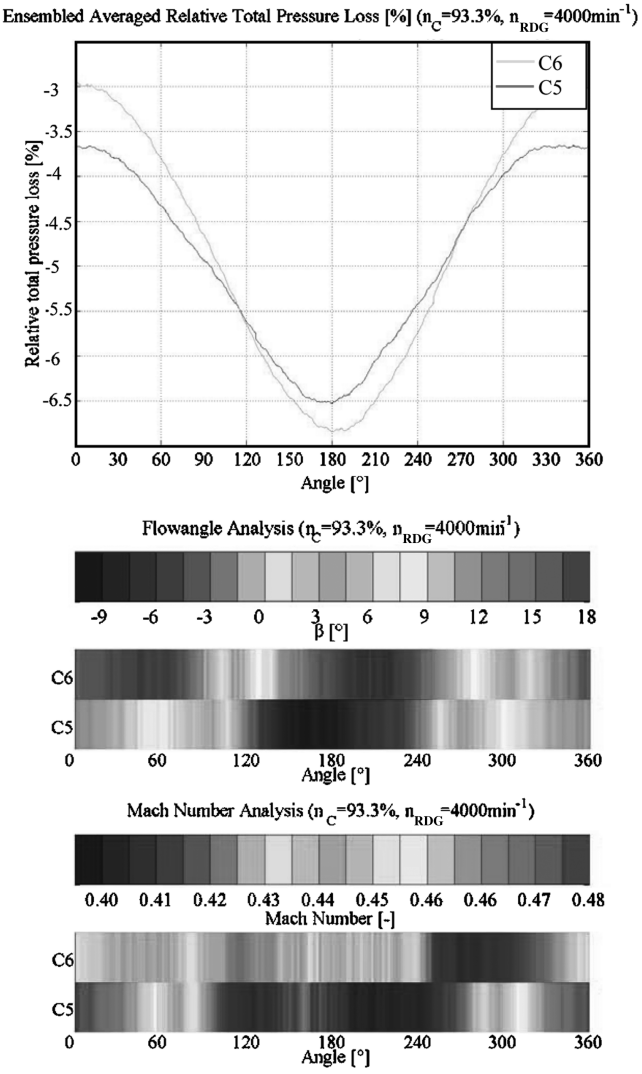

Fig. 4 Different total pressure inlet distortions (P2).

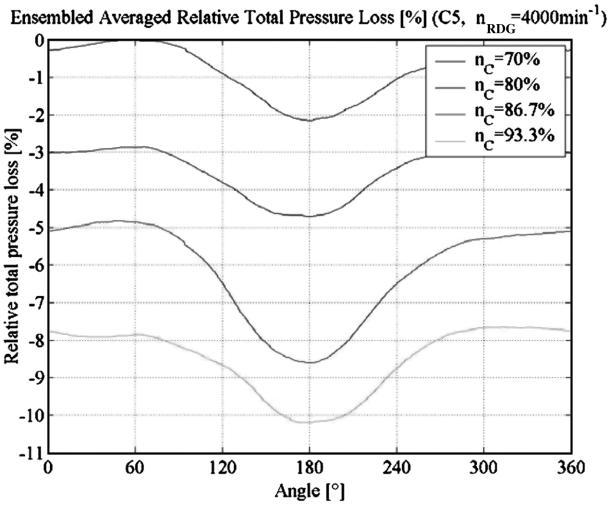

Fig. 5 Different compressor spool speeds (P1, C5).

superposed. With increasing compressor spool speeds, the axial flow is accelerated so there is not enough time for the flow to compensate for the static pressure gradients. The figure verifies that this effect dominates the intake flowfield at high compressor spool speeds.

The intensity of distortion is extremely dependent on the dynamic pressure and thus the axial flow velocity at the distortion generators.

For this reason, the setting of the throttle device affects the flow in the same way as the variation of the compressor spool speed, but rather more weakly.

B. Influence of RDG Speed

In Fig. 6, the influence of RDG speed on the ensemble-averaged total pressure distribution of C6 measured by P1 is shown (C5 can be read in [5]). The compressor spool speed is set to 93.3% with a throttle setting at the steady-state working line.

The speed of the RDG was varied as follows: $n_{\mathrm{RDG}} = 2000$ rpm, $n_{\mathrm{RDG}} = 4000$ rpm, and $n_{\mathrm{RDG}} = 6000$ rpm. The reference pressure is provided at C1. It is obvious that the relative total pressure loss is a function of the RDG speed. With increasing RDG speed, the maximum and minimum losses converge to a mean value. The effect is stronger at C5 than at C6 which has a more symmetric character. Here, the relative total pressure loss oscillates less at its maxima (max . $\pm$ 2%) around the mean value than at C5 (max . $\pm$ 3.3%).

The mean values of the total pressure losses of each configuration are very similar because they merge in one mean value. Thus, the mean total pressure loss of C5 is always slightly higher than that of C6. Because of the fact that the only difference between these two configurations is the RDG rotating direction, the higher total pressure loss at C5 is the consequence of an interaction of both distortion generators.

The difference of the mean total pressure losses between the two configurations is slight. Thus, it can be said that, in this case, the direction of RDG rotation has almost negligible influence. The result is that only the compressor spool speed and the distorted sector size are relevant variables for the mean total pressure loss. Indeed, the figure shows very different shapes of the total pressure distribution, meaning there are very different inlet flow conditions. These, however, have no influence on the mean total pressure loss and on the compressor behavior, as shown in Sec. IV.

With increasing distortion speed, the history of the total pressure distribution along the annulus changes from a rectangular (flow pattern at stationary objects) to a sinusoidal shape with a reduced pressure amplitude. The reason is an increasing cross acceleration of the flow due to the changing wake behind the RDG.

IV. Compressor Operating Behavior

A. Determination of Compressor Characteristics

The map of the undistorted inflow, configuration 1, is the reference for the evaluation of the effects of the combined coupled total pressure inlet distortion on the unsteady behavior of the compressor. To gain a systematic overview, four selected speed lines were analyzed: lower-, medium-, and high-speed range (70, 80, 86.7, and 93.3%). Distortion generator speeds were varied for configurations 3–6 to activate corotating or counter-rotating inlet distortions at 2000, 4000, or 6000 rpm. This enables an analysis of speed ratios commonly found in multishaft engines. A total of 56 different speed lines are thus provided for analysis and comparison.

Only the engine characteristics of selected configurations will be evaluated so as to not go beyond the scope of this analysis.

Defining the surge margin as a measure of the effects of the generated distortions is useful in only a few cases because the speed lines themselves and thus also the surge line shift to a lower flow rate and pressure rise. Even within a single configuration, there were significant flow rate and pressure ratio differences for the relevant parameter variations.

For this reason, Jahnen [1] already defined a loss value which expresses the decrease of the surge line pressure ratio and refers to the current surge line. This represents the stall pressure loss. In addition to the loss of the maximum pressure buildup, the changed reduced mass flow rate is also taken into account:

$$V = \frac{\Pi_{\mathrm{SL}} - \Pi_{\mathrm{SL,distorted}}}{\Pi_{\mathrm{SL,distorted}}} \tag{2}$$

The coupled inlet distortions of configurations 5 and 6 are of importance in the analyses.

All configurations, including the use of a distortion generator, show a loss in compressor pressure ratio, as well as a loss in mass flow rate around the surge line, whereas the pressure ratio around the capacity line remains almost unchanged. Some basic phenomena overlap and will be analyzed in the following based on various parameters.

B. Comparison of Configurations with Regard to Compressor Speed

As was shown in the preceding section, the various configurations themselves have the greatest impact on the flow ratio in the compressor inlet, thus changing the global operational behavior of the engine significantly. Figure 7 shows four speed lines for configurations 1, 2, 4, and 6 (C3 and C5 can be found in [5]) within the stable operating range of the engine characteristics. For the sake of clarity, the configurations with different rotating directions of the RDG were limited to two presentations. Configurations 3–6 are presented with a uniform RDG speed of 4000 rpm.

The shift of the speed lines to the left, to lower mass flow rates and pressure ratios (Π_V) due to the distortion generators is evident. The losses increase with increasing sector size. The smallest influence can be seen at C2 with an average mass flow and pressure ratio loss of between 1.5 and 2%. C3 and C4 generate a greater loss with an average of 4–7%. C5 and C6 have the greatest impact on the operational behavior. The loss of mass flow rate and pressure ratio varies from approximately 5% to nearly 10%. A direct comparison shows no significant differences in a large-scale diagram for either C5/C6 or C3/C4.

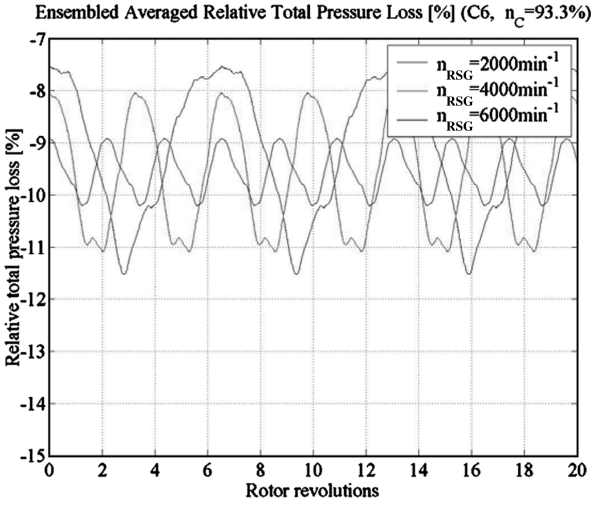

Fig. 6 Influence of different RDG speeds (C6).

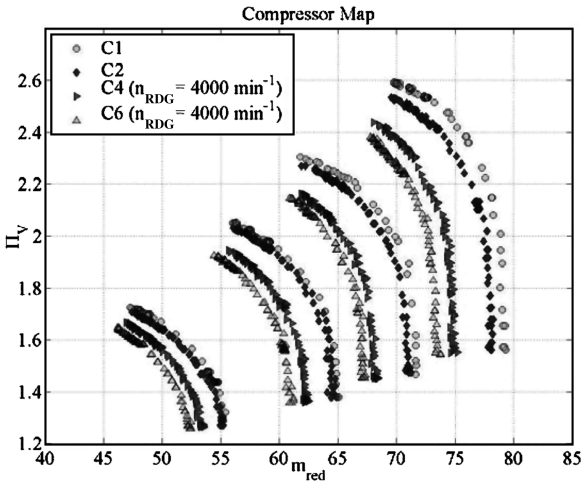

Fig. 7 Speed lines for configurations C1, C2, C4, and C6.

The degradation in performance was to be expected because the blocking of a sector of the intake channel to generate total pressure inlet distortions is very similar to a suction-side throttling. This results in an inlet flow reduction. Because of the inlet distortions, which generate a reduction of the flow cross section in the inlet, mass flow and axial velocity decrease. This leads to a change of velocity triangles, which in turn causes a reduction of the pressure ratio.

The effects of compressor speed on operational behavior reveal the increasing loss of performance for all configurations with increasing compressor speeds; this has also been demonstrated in the previous section. The loss of mass flow rate and increase of pressure ratio for each speed occurs due to the dynamic pressure at the distortion screens, itself a quadratic function of the flow velocity.

The increased reduction of the surge line with increasing compressor speed is also obvious. In contrast, there are hardly any dependencies on the degree of throttling. The loss of mass flow rate seems to be reduced to the same degree for all throttle settings with increased compressor speeds. The results of the pressure ratio analysis are similar. Changes of the curvature behavior and the speed line shapes were not observed.

The lowest surge line loss resulted under the sole influence of the steady-state total pressure inlet distortion of the steady-state distortion generator. The results of the analysis of C3/C5 and C4/C6, respectively, with a corotating RDG, are surprising. Here, the decrease of the surge line at C3 and C4 is generally stronger than for coupled distortion generator operation. This result indicates an interaction between the two distortion generators for coupled operation. The SDG seems to have a dampening effect, at least regarding the vortical flow generated by the RDG. A comparison of C3 and C5 shows the clearly greater losses at C3. Here, the results of Peters [9] and Longley [2] are reflected, which showed an earlier decrease of the surge limit for corotating total pressure distortions at lower distortion generator speeds. With regard to all speed lines, the loss at C3 is greater than the loss at C4. This allocation cannot be made for coupled inlet distortions of C5 and C6.

Figure 8 illustrates the unstable operating range in addition to the stable operating range. The 93.3% speed line in the aforementioned configuration 6 is depicted (C5 can be found in [5]). After the stability limit was exceeded, the compressor generated rotating stall. The throttle is then opened far enough for the flow to continue in a stable manner. The throttle must be opened much further for a stabilization of the compressor after rotating stall than at its initiation. The process of this hysteresis loop was recorded via steady-state data acquisition. Apart from the primary characteristics, the map shows the history of the quasi-steady-state operating points of the tertiary characteristics when the throttle is opened.

If rotating stall occurs at the compressor, the flow is quickly cut off and the operating point shows tertiary characteristics (deep stall). Full-span stall cells are generated within a few rotor revolutions after the stability limit has been exceeded.

It is notable that the compressor slips much further into rotating stall in the case of an undistorted inflow after exceeding the surge line than in the case of distorted inflow; the flow is also continuous for a much longer period. An explanation for this phenomenon could be the decreased engine performance for operation with inlet distortion which causes a less severe cutoff of the flow. In addition, the loading of the plenum on the pressure side is lower due to the decreased performance in the case with distortion. This is the reason for the lower counterpressure when the surge line is exceeded.

C5 and C6 differ only with regard to the RDG rotating direction. Even though the steady-state characteristics show no difference between C5/C6 the quasi-steady-state characteristics show considerable differences. When distortion generator speeds are varied, the position of tertiary characteristics changes much more significantly for corotating inlet distortions (C5) than for counter-rotating distortions (C6). These results correspond to the observations regarding the decrease of the surge line where the history of the counter-rotating distortions was more constant.

C. Influence of RDG-Speed

Figure 9 shows the effects of the distortion generator speed on the 93.3% speed line of C5 (C6 can be found in [5]). The RDG was set to 2000, 4000, and 6000 rpm. The absolute as well as the reduced mass flows increase with increasing distortion generator speeds. In contrast, the distortion generator speeds have a negligible effect on the compressor pressure ratio. In addition, observation of the primary characteristics of both configurations shows that the relative losses increase with increasing compressor speeds in spite of the increased engine suction behavior.

At C5, the average loss of the reduced mass flow for all speed lines and throttle settings is approximately 0.5% for a reduction of the distortion generator speed from 6000 to 4000 rpm. The maximum distortion generator speed of 6000 rpm is the reference figure due to the lowest impact. In case of a further reduction to 2000 rpm, the loss is increased on average to approximately 1.5%. In comparison to the previous section, these observations correspond to the relevant analyses in which inlet distortions at the lowest distortion generator speed caused the greatest pressure variations in the compressor inlet.

Because the effects of the different inlet total temperatures on the reduced mass flows are almost negligible (maximum 0.1% of $n_{RDG} = 2000$ rpm to $n_{RDG} = 6000$ rpm), a similar picture is presented for the absolute mass flows. Almost identical losses are identified for the analyzed speed lines of configuration 6. It is also evident that the position of the steady-state operating points in the map is not a function of the RDG rotating direction, at least with regard to C5 and C6. No regularity could be demonstrated for the position of the stability line as a function of the distortion generator speed.

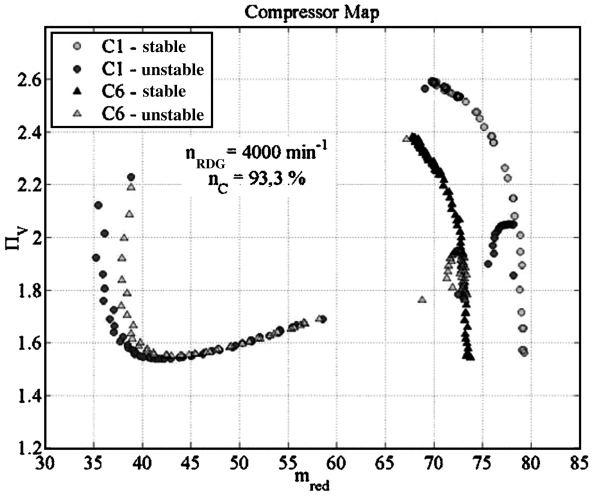

Fig. 8 Hysteresis (C1, C6).

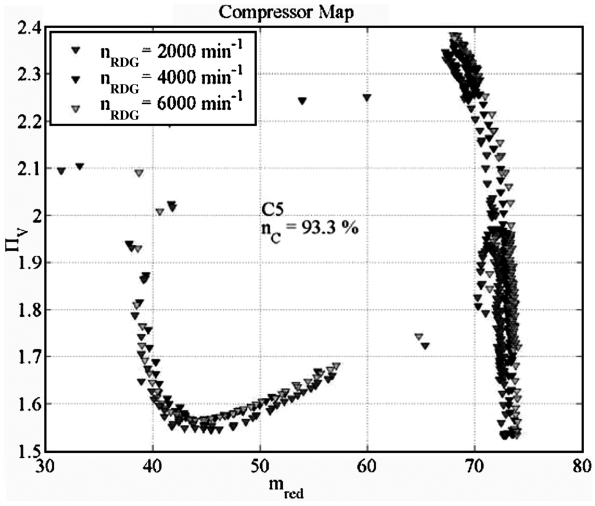

Fig. 9 Hysteresis at different RDG speeds (C5).

For increasing distortion generator speed, a decrease of the reduced mass flow of approximately 3–4% was identified for all compressor speeds. The maximum loss for the compressor pressure ratio is 1% on the 93.3% speed line. The absolute losses increase with increasing compressor speed.

Contrary to the stable operating range of the compressor, no systematic impact of the RDG speed on the operating behavior could be identified during hysteresis after a rotating stall was established. As previously mentioned, a transition to the unstable operating range at C5 and C6 is neither a function of the rotating direction nor a function of the RDG speed. The tertiary characteristics, however, show a trend similar to the behavior of the primary characteristics. Here, the impact at low RDG speeds is also greater and the flow cutoff of the compressor will be deeper as soon as rotating stall has been established.

V. Flow Analysis When the Stability Limit is Exceeded

A. Time Range Analysis

For the investigations at issue, the measurement data of five static wall pressure transducers, arranged in the compressor intake and along the circumference, were used. For most measurements, the sampling rate was 100 kHz. At such a high sampling rate, there are specific requirements regarding the processing and evaluation of the signals. First, the synchronous recording of the various measuring channels must be ensured to prevent data shifts. Second, the correct mapping of all occurring frequencies must be secured. A summary of signal analysis within the time range is included in [5].

Figure 10 includes a short insight into the complexity of the pressure signals received. In this figure, the example of a recording of a 10 deg wall pressure transducer shows the superposition of several signals. The transition from stable flow to unstable flow is recorded for configuration 6 at the 86.7% speed line. The beginning of rotating stall can be identified starting at rotor rotation 17 in the upper figure. Before this, the periodic part of the enforced, combined total pressure distortion can be clearly identified. The RDG impresses a rotating distortion of 2000 rpm on the flow. The second figure from the top shows more than one distortion revolution within the rotor revolutions 4–12. Further section refinement clearly reveals the vibrations representing the compressor speed between revolutions 6–9. The bottom figure finally shows the 87 deflections of the blades of the first rotor within one revolution. As can be seen, even this simple investigation of the time signal yields much information which has to be interpreted. The use of a low-pass filter upstream of the A/D converter prevents the corruption of data due to higher-frequency distortion signals. Nevertheless, other histories may superpose these visible histories and be subject to regularities which can be identified only by means of a frequency spectrum analysis.

On the other hand, Fig. 10 also shows that some vibrations may be detrimental to the investigation of other issues. This is best illustrated by the compressor speed. Because of its superposition, the history of the inlet distortions is affected considerably. The difficult solution consists in the application of bandpass and bandstop filters used to filter specific frequencies from the signal. A sampling rate of 100 kHz causes considerable problems in generating a bandstop with a cutoff frequency of only a few hertz [5].

1. *Development of the Distortion*

Axial compressors such as in Rig212 are also termed “tip stallers” due to the aforementioned high aspect ratio. With regard to these tip stallers, the flow is at first separated around the outer casing, initially leading to the so-called part-span stall. In the case of a narrow cascade pitch, that is, contiguous blades, the flow can follow the blading contour more easily than in the case of a larger cascade pitch. The cascade pitch at the hub is smaller than at the casing. This leads to a more favorable flow redirection at the hub and a reduced redirection of the flow at the casing, which in turn means less favorable angles of incidence with respect to the next stage. Because of the reduced redirection caused by the greater cascade pitch at the casing, the blade is designed with a greater camber. However, this also means a greater

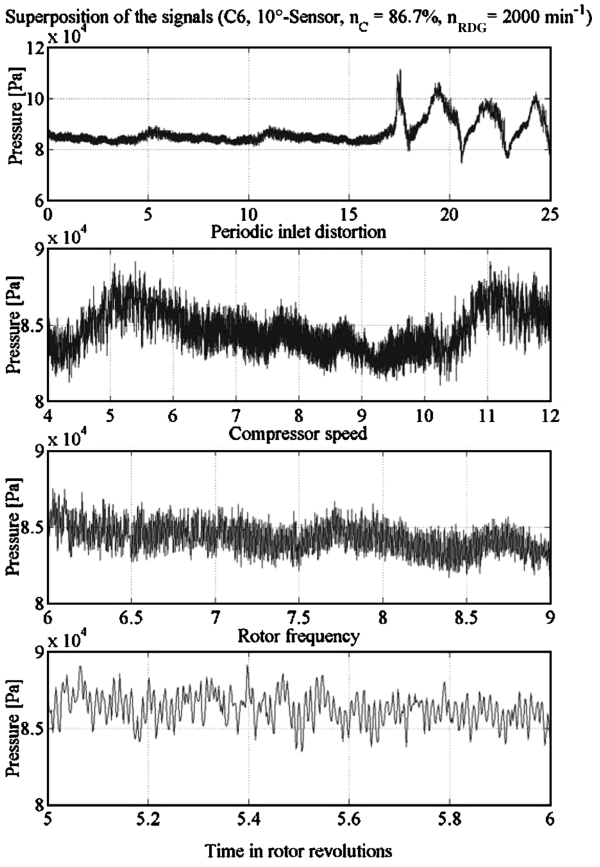

Fig. 10 Superposition of pressure signals.

flow deceleration, increasing the risk of stall. The tip flow, together with the secondary flow phenomena, for example, the vortex through the radial gap, is thus inherently more unstable than at the hub section.

An infinite number of blades without friction would be the ideal case. Friction and weight are the reasons for limiting the number of blades. If the cascade pitch increases (e.g., in the casing section), an infinitely large cascade pitch can, in extreme circumstances, result in an airflow around a single airfoil causing no redirection of the flow.

The analysis of the pressure transducers set up circumferentially can assist in investigating the behavior of the flow in the compressor after reaching the stability line. When stall at the compressor is imminent, it is possible to identify the specific phases in this overall process called stall inception. After stationary operation, a short period of flow oscillation may occur before the formation and growth of a stall cell. The prestall and cell-formation phases are of primary interest in this regard. The categorization is as follows: a) stable operation; b) prestall: period immediately before stall inception. Compressor operation is stationary. However, distortions of small amplitude (∼1%, modal waves) may be generated. These distortions are very small vs paragraphs c and d; c) stall inception: transient process of axisymmetric flow conditions showing small distortions to rotating stall showing great distortions, their amplitudes changing over time. The shortwave distortions (spikes) discovered by Day and Freeman [10] qualify for this category; and d) fully developed rotating stall: distortions of large amplitude are generated (50–100% of mass flow fluctuation). In contrast, the amplitude changes of the distortions are not significant.

It has proven very difficult to categorize regions a–d precisely. This terminology, however, enables unequivocal communication. The developmental process of rotating stall is illustrated in Fig. 11. After exceeding the surge, line spikes initiate the generation of rotating stall. After approximately three revolutions, the flow separation has developed and the fully developed cells can be identified by means of recurring pressure variations. The prestall phase cannot be identified within the time range. It is possible that it

does not even exist because it is spikes and not modal waves which initiate the process. The quasi-stable prestall region, however, is often the most interesting region because stable operation is the design target, and this aim has not been achieved as soon as stall has been initiated. For this reason, Tryfonidis et al. [11], focused on the prestall inception dynamics of the HPC. Via the traveling wave energy analysis (TWE), they showed that there are rotating prestall waves with small amplitudes around all investigated HPCs. These strongly depend on the reduced compressor speed. This suggests that the dependency of the wave structure is a result of compressibility effects at higher circumferential speeds.

In the following, the development process of rotating stall inception at the compressor intake is investigated via wall pressure transducers arranged circumferentially. The transducers are installed directly in the intake cross section of the first rotor. This is a very important fact regarding the conservation of the stall cell structure over the course of the pressure history. Figure 11 shows the flow behavior of configuration 1 as an example, as well as configurations 5 and 6, with a rotating distortion generator speed of 4000 rpm at the compressor intake when exceeding the stability line at the compressor speed of 70 and 93.3%.

The stall behavior of Rig212 hardly differed from that in the investigated configurations. The compressor exhibited stall within a few rotor revolutions following the occurrence of spikes. In the prestall phase before instability, the periodic effect of the RDG can be identified at C5 and C6. Effects on the stall behavior and the structure of the developing stall cells could not be observed. However, varying levels of the respective instability could be identified.

The sudden initial occurrence of flow separation was normally detected by the 180 deg sensor. The stall cell moves at approximately 60% of the compressor speed and rapidly grows within one or two revolutions. After two to three more revolutions, rotating stall has been established. The speed of the cell is reduced to approx. 45% of the compressor speed and its width is approximately 50% of the annulus. The individual spike speed values for the configurations investigated are included in Table 1. This is the typical behavior for stall via spikes which generates a rapidly revolving part-span stall cell within a very short period of time. This cell rapidly develops into a slowly rotating full-span cell which is the cause for the deep stall illustrated in the compressor map.

The effect of the SDG is indicated in the fact that a detection of the first stall cell correlated to various circumferential positions of the SDG in various test series. This was never the case with respect to the undistorted reference. This is a clear indication of the validity of the spike model; the spikes are generated by the shortwave distortions in the otherwise axisymmetric flowfield of the intake channel.

The line in the upper right illustration of Fig. 11 identifies the propagation speed of the developing stall cell at various positions in the annulus. This is apparently a part-span stall cell changing rapidly into a full-span stall cell. A comparison of the measurements of the static wall pressure transducers, including the results of the multiple-hole probes, shows a slight delay from the casing to the hub at the start of the stall. Separation therefore begins at the blade tip. When investigating the results of the sensors at the circumference, it is clear that compressor stall occurs exclusively in one cell rotating around the annulus.

Although experience shows that wall pressure transducers arranged circumferentially at the compressor intake are best suited to signal the first indications of flow destabilization, all data records evaluated are identical in that no indication of imminent stall can be detected within the time range.

Figure 12 shows the beginning of rotating stall via the axially arranged wall pressure transducers. This is configuration 1 at a compressor speed of 93.3%. The scaling was identical for all data records shown to ensure an improved comparability of the various pressure levels along the compressor.

The result is unexpected but representative of all configurations. Neither the typical speed-sensitive behavior of multistage machines nor the typical behavior of HPCs operating in the compressible regime could be observed; this is explained in short in the following.

In multistage compressors, the flow is cut off initially in the section in which the dynamic load is highest. Depending on speed and intake conditions, this can be the first, middle, or rear stages. The graphic display of the axial measurement, however, indicates that the aerodynamic load of the individual stages when reaching the surge line is approximately identical because rotating stall commences simultaneously throughout compressor.

The distortion postulated in the hydrodynamic Greitzer–Moore model [13] has the same characteristics which (resulting from the equation of continuity at incompressible flow) is instantaneously propagated through the compressor and for which axial speed is not a function of the length. Apart from this, the results are identical to those from Cumpsty [12] who mentioned axial propagation of the generated full-span stall cell (vertical line). The individual stall cell extends almost to the compressor exit; unfortunately, this cannot be identified precisely at the exit. In addition, the width of this cell is identical at all stages and its speed in the compressor does not change.

After the short stall inception phase, the considerable pressure loss of the rear stages during fully developed rotating stall is remarkable. This result correlates to the enormous performance loss of the compressor which, following commencement of rotating stall, exhibits tertiary characteristics. Although the performance losses are relatively low during the transition from primary to secondary characteristics, they are considerably more dramatic for the transition to tertiary characteristics. The reason for this is the generation of a large stall section (the registered full-span stall cell) covering the entire blade channel in the radial direction. The flow can no longer compensate itself along the circumferential direction due to the narrow spacing of the blade rows downstream. Thus, the stall section extends to cover the entire compressor axially, causing an accumulation of the performance losses of the individual stages.

Configurations 5 and 6 show the same behavior as C1 regarding compressor and RDG speeds. However, before the start of rotating stall, the effects of the rotating inlet total pressure distortions and their solely axial movement through the compressor can be identified during stable operation.

The axial positions of the wall pressure transducers between the stages affect the measured pressure history. The sensor in the compressor intake is therefore installed preceding the first rotor; it shows the typical pressure history of rotating stall measured above the leading edge of the blading. The other pressure transducers are also positioned preceding the respective following stages. They are also installed behind the previous stage. Thus, the section affected by the flow separation cannot show the same extent of the pressure increase along the compressor as the undistorted sections of the flow. Therefore, the pressure level of the flow within the stall cell decreases with every further stage vs the remaining section of the annulus.

2. *Characteristics of Fully Developed Rotating Stall*

The structure of the stall cells in the illustration strongly depends on the position of the transducers. The question arises in Fig. 11 as to which cells are stall cells and how the flowfield can be interpreted physically. The pressure transducers in the compressor intake are installed directly at the leading edges of the blades of the first rotor.

A rotating stall cell is a section of separated air flow which can be identified in the pressure history by means of a very noisy signal. In Fig. 11, this is illustrated left of the pressure maximum along the falling slope to the pressure minimum. The stall cell represents a blocking in parts of the annulus resulting in a retained flow. This causes a diversion of the flow resulting in a pressure increase in the recording. If the cell passes the transducer, the pressure decreases again, the flow stabilizes, and the process begins anew.

Before and following the complete revolution of a stall cell, the flow at the blading around the transducer is stable. This is established by means of pre- and postseparation pressure level comparisons. The ratio of the cell length to the total period length results in the relative extension. The results from Rig212 vary between approximately 55 and 62% of the relative extension. The process is periodic. However, due to the extreme flow conditions at the compressor blading, it is subject to variations in the circumferential extension of a cell. The

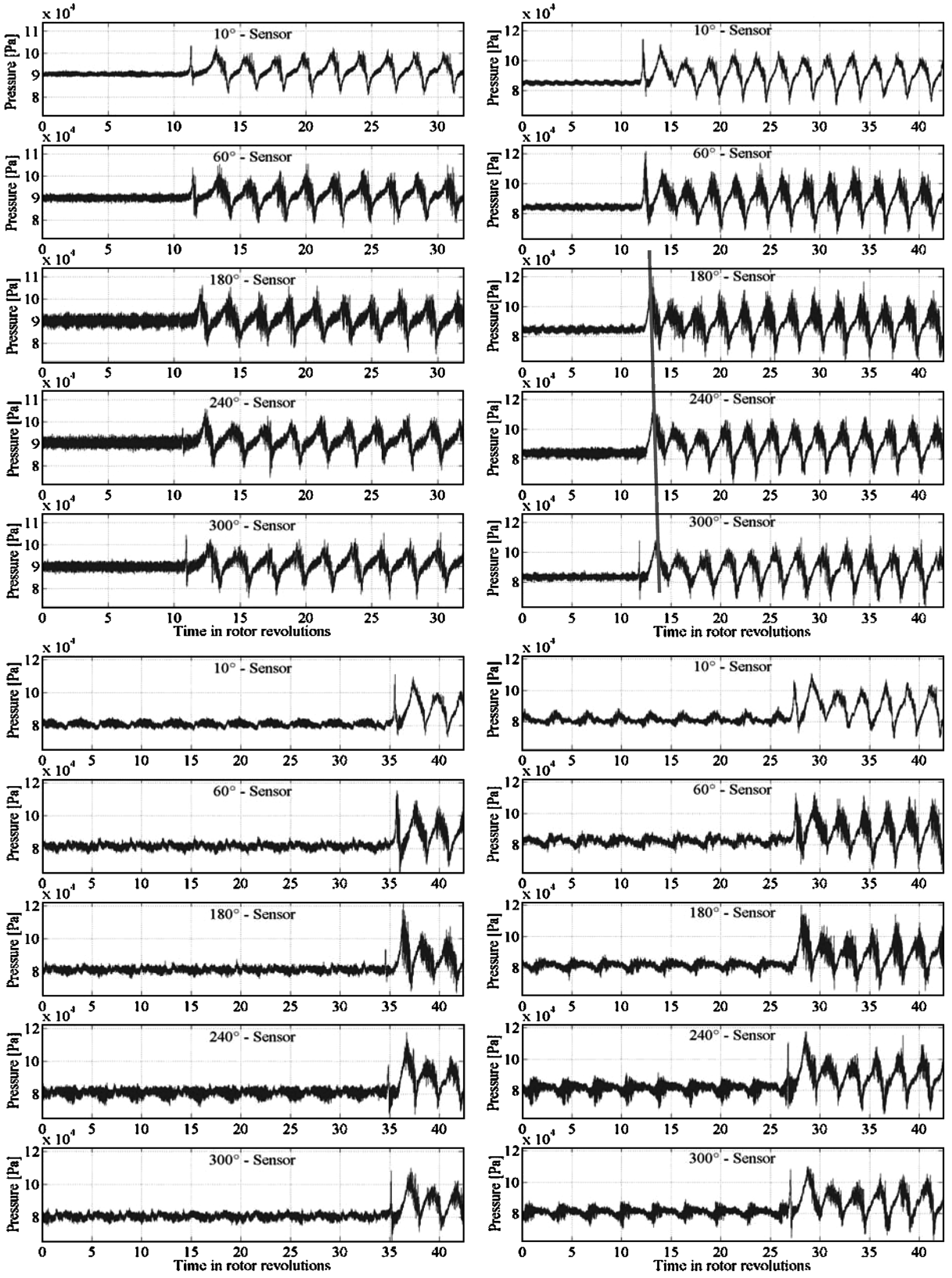

Fig. 11 Top left: C1, $n_C = 70\%$; top right: C1, $n_C = 93.3\%$; bottom left: C5, $n_C = 93.3\%$, $n_{RDG} = 4000$ rpm; bottom right: C6, $n_C = 93.3\%$, $n_{RDG} = 4000$ rpm.

results of the three-hole probes positioned at level 1.1 are a first indication that the separated flow sections do not extend very far into the inflow of the first rotor. Although large pressure variations are registered during the passing of the stall cell at the lateral pressure holes 2 and 3, analog to the static wall pressure transducers, hole 1 only shows a diversion of the flow [5].

As for stall inception, an investigation of the characteristics at the circumference of the compressor intake is performed for fully developed rotating stall. For a better overview, the characteristics, calculated using the measured data and included in Table 2, were compiled for configurations 1 (reference configuration), 5, and 6. The significant characteristics include the total stall process period,

Table 1 Speed of spikes vs compressor speeds

Speed of spike, % n_C	$n_C = 70\%$			$n_C = 80\%$			$n_C = 86.7\%$			$n_C = 93.3\%$		
C1	58			64			63			58		
n_{RDG}, rpm	2000	4000	6000	2000	4000	6000	2000	4000	6000	2000	4000	6000
C5	58	58	64	64	65	54	62	62	59	58	54	65
C6	58	62	61	65	65	53	64	65	56	62	65	65

pressure amplitude, propagation speed, and the extension of a stall cell within the annulus.

To facilitate a better comparison, the period of the complete rotating stall process was calculated and not expressed in terms of rotor revolutions. There were variations regarding the rotating stall period and the recovery of the flow. In general, it was observed that the time period in which the compressor was operating with stall characteristics decreased in all configurations with increasing compressor speed. Furthermore, the direction of rotation of the RDG affected the stall characteristics. For corotating inlet distortions (C5) the rotating stall period for all investigated speed lines and distortion generator speeds was approximately 90 and 80% of the reference configuration 1 for C6.

After the stall inception phase, full-span stall cells are generated within a few rotor revolutions in all investigated configurations. The compressor then operates with tertiary characteristics. The recovery of the flow, however, is speed sensitive. Initially, part-span stall cells are generated at low compressor speeds before flow recovery. By contrast, the phase during which the compressor operates in stall ends as abruptly at high compressor speeds as it began. Figure 13 shows the pressure history of the 10 deg transducer with respect to a complete throttle cycle for C1. There is a clear division into two sections: one section including full-span stall cells, followed by a section with part-span stall cells. The period in which the compressor operates with full-span stall cells is almost identical for all configurations. Because the throttle settings during the hysteresis loop remain constant for all configurations and are only a function of time, it can be concluded that the operation of the compressor with the tertiary characteristics with full-span stall cells depends largely on the throttle setting and not on the compressor speed.

A speed dependency was established with the amplitude of the stall cell pressure variations. Because of the higher potential energy in the plenum on the pressure side, the pressure variations increase as expected with increasing compressor speed. This effect of deeper stall was established previously in the observations of operational behavior. The pressure amplitude increases from the 70% speed line by approximately 50% to the 93.3% speed line in all investigated configurations. No effects of the generated distortions on the stall cell pressure amplitudes were observed.

The propagation speed of the fully developed stall cells was nearly identical for all configurations of one speed line. Merely a slight speed decrease from 46% of the compressor speed to 43% was observed with increasing compressor speed. This, however, is directly related to the size of the stall cell in the annulus. The ratio of the circumferential expansion of the cell to the total circumference results in the relative extension. The results vary between approximately 55% ($n_C = 70\%$) and approximately 62% ($n_C = 93.3\%$) of the relative extension. This corresponds to the observation made earlier. During the growth of larger stall cells, they become slower because more energy must be transformed for each revolution. This effect can also be identified in comparison with the smaller part-span stall cells which generally revolve in the annulus 1.5 times as fast as the larger full-span stall cells. The growth of the cells with increasing compressor speed correlates to the increase of the pressure amplitudes.

The stall process is periodic. Following their generation, an alteration of the shape and characteristics of cells is barely noticeable. However, due to the complex flow ratios at the compressor blading, there are, nevertheless, variations in width. For this reason, this quantity is not included in Table 2.

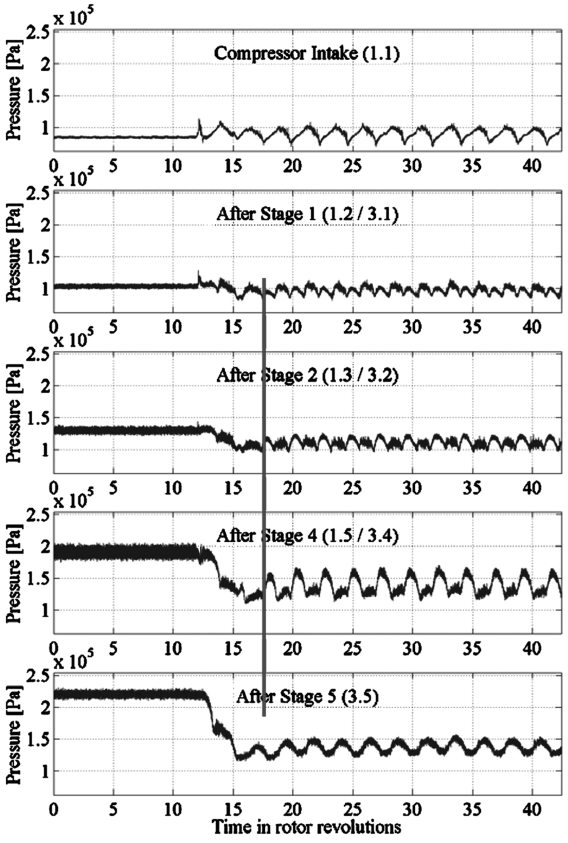

Fig. 12 Start of rotating stall along the compressor for C1 (n_C= 93.3%).

B. Frequency Range Analysis

1. Detection of Stall Predecessors

Several more or less successful analysis methods were developed for the detection of stall predecessors. These are listed in the following. The evaluation within the spectrum shows significantly more flow details than a pure time range analysis. Even the gradual

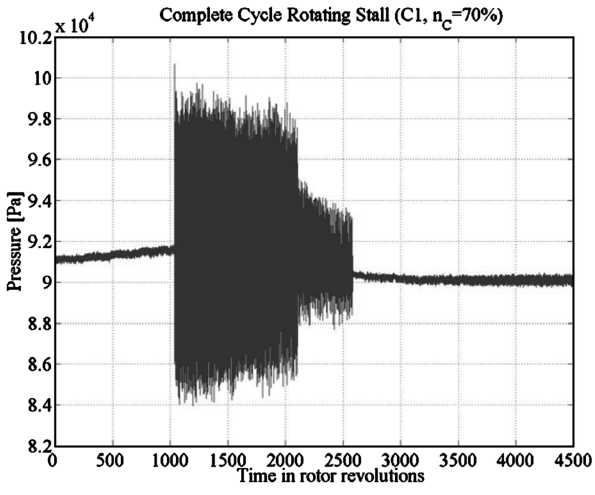

Fig. 13 Complete rotating stall process (C1, $n_C = 70\%$).

Table 2 Characteristics of fully developed rotating stall

$n_C = 70\%$	C1	C5			C6		
n_{RDG}, rpm		2000	4000	6000	2000	4000	6000
Period, s	9.7	7.8	8.5	8.7	8.6	9.1	9.1
Quantity, kPa (pressure amplitude)	18	22	21	18	19	17	20
Speed, % n_C	45.8	45.9	45.9	45.9	45.9	45.8	45.8
$n_C = 80\%$							
Period, s	9.6	7.9	8.4	7.1	8.6	9	8.6
Quantity, kPa (pressure amplitude)	24	26	27	25	27	25	28
Speed, % n_C	43.5	46.9	43.5	43.5	43.5	43.4	43.4
$n_C = 86.7\%$							
Period, s	9.4	6.9	6	7.5	8.1	8.8	7
Quantity, kPa (pressure amplitude)	27	27	30	27	29	29	29
Speed, % n_C	43.4	43.3	43.3	43.3	43.3	43.3	43.3
$n_C = 93.3\%$							
Period, s	6.9	6	5.8	7.9	6.1	7	8.2
Quantity, kPa (pressure amplitude)	30	29	29	34	32	32	33
Speed, % n_C	43.2	43.1	43.1	43.1	43.1	43.1	43.1

increase of modal waves as an indication of a beginning instability was rarely detected within the time range.

C. Windowed Fourier Transformation Analysis

The first procedure is the short-time Fourier transformation (STFT). Spectrograms were established for C5 and C6 ($n_C = 93.3\%$, $n_{RDG} = 6000$ rpm) (Fig. 14). The length of the window was 50 ms with an overlap of 49 ms. A modified Bartlett–Hanning window was used for the window function, illustrating a weighted linear combination of the Bartlett and the Hanning window. It depicts a bell shape similar to a normal distribution with asymptotic slopes at the sides. The length of the respective discrete Fourier transformation (DFT) was set to 65,536 points. An ideal frequency resolution was achieved with this relatively large window width and DFT length. The quantitative determination of the respective amplitudes is dependent on sensors and is of no relevance in this investigation. The resulting values would be confusing for the observer; the physical interpretation of these values can be explained simply with the energy contained in the signal. It is only the qualitative history which is of interest. The amplitude axis was therefore scaled identically for identical speed lines.

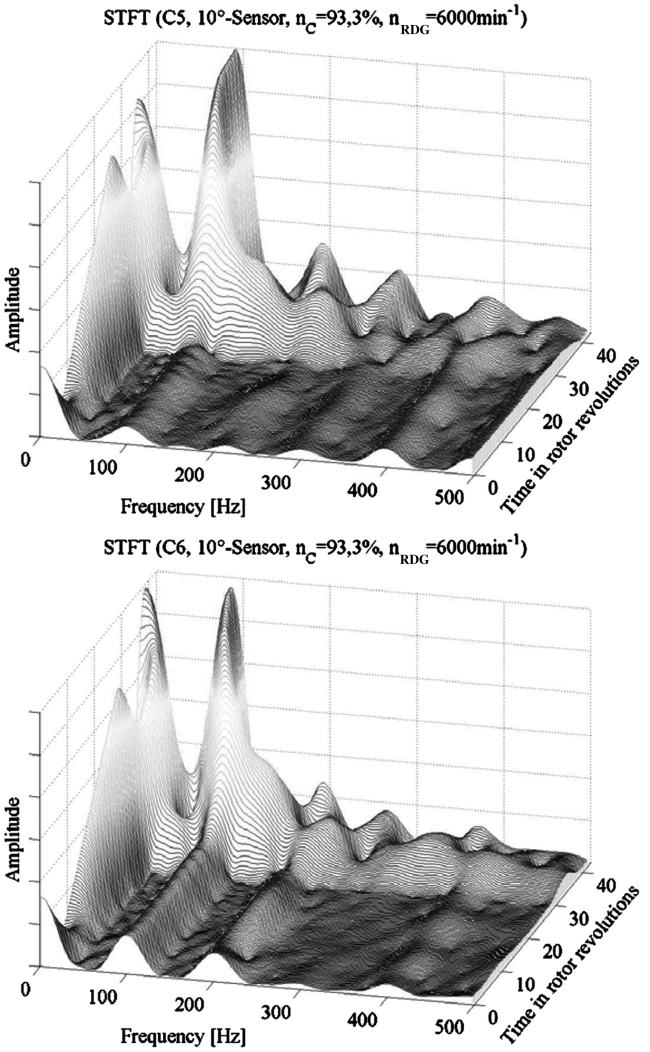

Fig. 14 Start of rotating stall at the compressor intake for C5 (top) and C6 (bottom) ($n_C = 93.3\%$; $n_{RDG} = 6000$ rpm).

Modal waves and spikes move within the annulus at a speed that is below the compressor speed. For this reason, a detailed investigation of the low-frequency range should be performed at first.

The figures show an enormous increase in amplitude at the frequencies at which rotating stall occurs (see Table 2). At the beginning of the instabilities, their first harmonic, which is characterized by the propagation speed of the cells, dominates the spectrum. The evaluation of the 70% speed line shows a further clear deflection at approximately 150 Hz for all configurations. This is probably a harmonic of the rotating stall cell. However, this effect is speed sensitive because the amplitude of this vibration decreases with increasing compressor speed. At the 93.3% speed line, it can hardly be distinguished from the other fundamental frequencies and harmonics.

In the stable range before rotating stall, the compressor speed and the RDG speed are shown. The compressor speed expressed as a frequency is approximately 215 Hz for the 93.3% speed line in the first harmonic. These values are dependent on the intake conditions and are selected to regulate speed to the desired values. For a distortion generator speed of $n_{RDG} = 6000$ rpm, the independent value is always 100 Hz.

The speeds are clearly visible on the right-hand side of Fig. 14 at 100 or 215 Hz. The figures give the impression that rotating stall develops at these speeds. This, however, may be deluding because the overlapping presentation allows a continuous development of the spectrum within the time range.

At 0–50 Hz, a phenomenon occurs and increases continuously up to the beginning of the instability. These are, however, pseudofrequencies generated due to overlapping which show an increase of rotating stall. As already mentioned, the correct resolution of the existing vibration requires the investigation of several periods in one analysis window. Because of the continuous shifting of the analysis window, the beginning of rotating stall is also evaluated. However, no full revolution is included thus far. The STFT shows a constant value at 0 Hz which increases with increasing pressure signal. As soon as rotating stall has developed and is included entirely in the analysis window, these pseudofrequencies vanish. Unfortunately, this problem is unavoidable because the STFT allows either a high-

frequency resolution or a high-time resolution. At the same time, an interesting frequency range is superposed, thus possible indicators within this range cannot be identified. There is a similar problem regarding the frequencies of the compressor and RDG speeds because a vast amount of the frequency ranges is superposed by their first harmonics.

Overall, the investigation of the data records including the STFT revealed no changes of the signal characteristics. Rotating stall emerged suddenly without advance warning in all investigated configurations and at all speeds. It was preceded merely by a noisy spectrum with rather weak compressor and RDG rotor frequency characteristics. In addition, no increase of characteristic frequencies was observed in the ranges before stall, nor did the investigations of the high-frequency sections including the Nyquist frequency show any increases.

D. Traveling Wave Energy Analysis

One can argue that there are modal distortions in spite of spikes but that their amplitudes are too small to be detected. This is possible because Tryfonidis et al. [11] compared the data of nine HPCs during stall inception. They developed the traveling wave energy model as a stability analysis for the detection of prestall waves before the beginning of stall. It became apparent that rotating stall preceded the beginning of surge at each HPC. This in turn was preceded by rotating waves with low amplitudes up to several hundred rotor revolutions before the beginning of the instability. These rotating waves were found to be a function of the compressor speed with compressible effects becoming strongly visible under full load. The idea was motivated by the hydrodynamic theory from Greitzer and Moore [13] and their model description.

This method is based on the assumption that, before rotating stall, the energy contained in the flow must increase. However, the distortion amplitudes are so small that they cannot be detected within the time range. A spatial Fourier transformation is thus the first calculation step in this method. The circumference-dependent Fourier coefficients are calculated using the circumference instrumentation data. Up to seven pressure transducers are available for this evaluation. Tryfonidis et al. [11] demonstrated that the circumference Fourier transformation alone, and the evaluation of the values and phases of the first and second harmonic coefficients as introduced by Garnier et al. [14], are not sufficient for an early detection. Modal waves with small amplitudes in particular can only be detected with great difficulty or not at all by means of the circumference FT.

To obtain a measurement of the energy content of the distortions, the power spectral density (PSD) is calculated for the sequence from the first or second harmonic Fourier coefficients, determined by means of the circumference analysis. A time window is selected for the input of all first or second harmonic Fourier coefficients. This results in a PSD for each window. Because of the complex coefficients, the PSD is two sided.

The difference between the positive and the negative part of the spectrum is established (differential power density spectrum). This results in the elimination of static waves because they occur equally in the positive as well as the negative part of the spectrum. Rotating waves, on the other hand, only occur in one-half of the spectrum, depending on whether they are co- or counter-rotating. This difference is named by Tryfonidis et al. [11] as the energy of rotating waves because the stationary part is eliminated by calculating the difference. The analysis window is then shifted and the differential power density spectrum is calculated anew. Subsequently, integrations are calculated for each difference section.

In this manner, each spectrum is reduced to a single integral TWE value. Plotted versus time, this gives a development of the energy of rotating waves which is well suited as an advance warning indicator. The level of the wave energy increases until rotating stall starts. If the TWE value exceeds a certain limit, the compressor reaches the unstable range. This calculation is therefore also suitable for regulation systems monitoring operational behavior. By calculating the TWE value, all information about the modal wave itself is lost because only one value remains from each spectrum due to integration.

Because of the expected energy increases in the low-frequency range, the superposition of the compressor and RDG rotor frequencies may prevent a possible detection of rotating waves. For this reason, these frequencies were filtered digitally out of all investigated data records.

For each speed line, the integral TWE value was established for the first and second harmonic of the circumference FT up to 180 rotor revolutions before the beginning of rotating stall. After flow separation, the TWE values exceed the values in the stable range by several orders of magnitude. This explains why the commencement of stall is not presented. The integration limits for the time window used were 10 ms.

Figure 15 shows the TWE value for undistorted configuration 1 at which the respective rotor frequency was filtered. With respect to the 70% speed line, an increase of the TWE value is registered for the first as well as the second harmonic approximately 60 rotor revolutions before rotating stall.

With respect to the 93.3% speed line, a sudden increase of this value is observed only for the second harmonic between revolutions 60 and 140; before this point, identification not possible. In contrast, with the exception of the range directly before rotating stall, the first harmonic shows no deflections exceeding normal variation.

In contrast to C1, no deviations can be observed at C5 and C6 within the combined distortion range. These graphs are not illustrated in this article for lack of space. They are included in [5]. First, the dampening effect of the SDG is responsible for this. Second, however, there is a clear dependency on the RDG speed. This influence can be attributed to the harmonics of the rotating inlet distortion because only the fundamental frequency was filtered out. Each further filtering of certain frequency ranges would also distort the original signal. In so doing, pseudofrequencies could be generated that do not actually exist. In addition, there is a risk that exactly those frequency ranges are also filtered out in which the prestall waves increase.

The HPCs investigated by Tryfonidis et al. [11] were operated without any inlet distortion. However, the comparison of configurations 1, 5, and 6 shows that these distortions alone affect the results. Peters [9], who analyzed the effects of the rotating inlet total

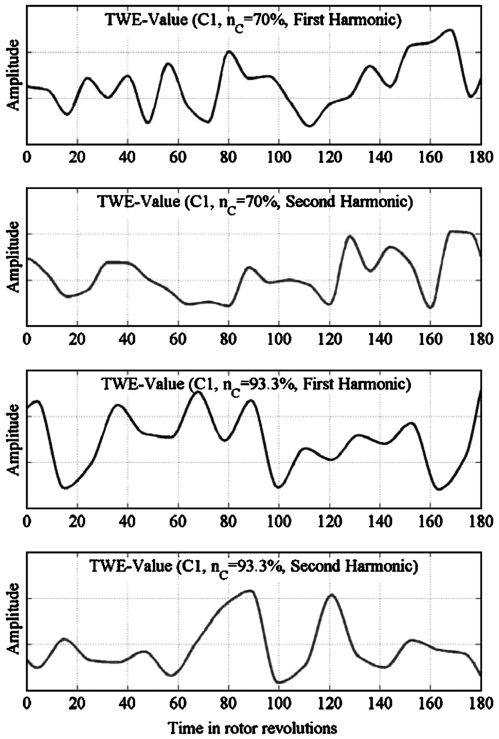

Fig. 15 Integral TWE value at C1 [$n_C = 70\%$ (top), $n_C = 93.3\%$ (bottom)].

pressure distortions using Rig212, divided up the investigated frequency range. This method was unsuccessful because the TWE value increased only at random speed ratios. No regularities or dependencies could be established. Peters also used hot-wire probes at the mean radius directly in front of the first rotor. The investigations in question are based on the data of wall pressure transducers positioned directly above the leading edge of the blades.

E. Wavelet Transformation Analysis

Uhlmann [15] tested a method for the early detection of aerodynamic instabilities using various compressors. By means of the wavelet analysis, he was able to identify stall predecessors. For this, he only needed a maximum of two pressure transducers in the compressor intake. Another example using wavelet transformations for the study of aerodynamic instabilities can be found in Brown and Sawyer [16].

The aforementioned Fourier transformation types reflect the frequency content of a time series. However, time aspects are lost. Wavelet analyses, on the other hand, differ characteristically. They include a resolution of both the time and the frequency axis.

In contrast to the Fourier transformation, the window of the wavelet transformation is scaled. This is particularly important with respect to signals consisting of mixed frequencies and signals whose spectra change with time.

Only a single temporary curve (wavelet) is used, which is subsequently shifted and scaled during the transformation. Nearly any function can be used as the basic function of the wavelet transformation, which is generally defined as the convolution of the signal $x(t)$ with function ψ. Further information on the wavelet transformation is included in [5].

The top half of Fig. 16 shows the spectrum of the continuous wavelet transformation for C1 at the 70% speed line. At this point, there is an increase in the amplitudes of the spectrum (dotted ellipse) below the filtered rotor frequency, approximately 150 rotor revolutions before the beginning of rotor stall. The result for the 93.3% speed line is illustrated in [5]. The identification of stall predecessors was more difficult at this speed line, even using the TWE. This can be confirmed for the continuous wavelet transformation. Approximately 250 rotor revolutions before commencement of stall, there is a slight increase in coefficient amplitudes (dotted ellipse), recognizable due to the appearance of lines. This indicates a different mechanism than modal waves, which do not

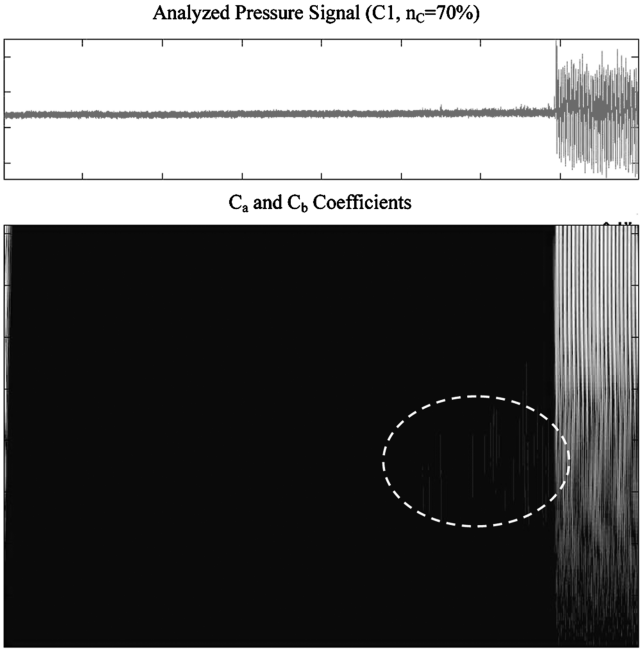

Fig. 16 Continuous wavelet transformation for C1 ($n_C = 93.3\%$).

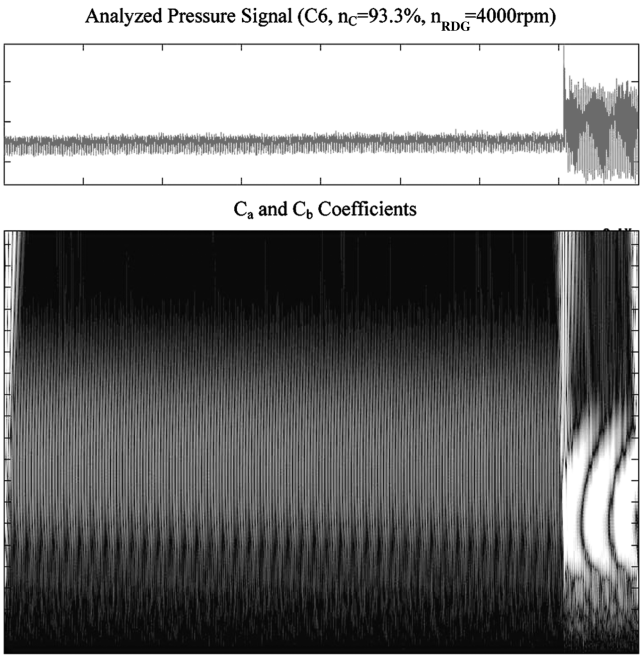

Fig. 17 Continuous wavelet transformation for C6 ($n_C = 93.3\%$, $n_{RDG} = 4000$ rpm).

revolve as rapidly in the annulus. These characteristics, however, are not significant enough to calculate a threshold value, indicating the unstable operating range.

No indications of stall predecessors were detected for configurations 5 and 6. The RDG in particular causes such intense spectrum noise that any interpretation of certain frequency ranges would be pure speculation. Figure 17 shows the evaluations of the mean distortion generator speed ($n_{RDG} = 4000$ rpm) for the 93.3% speed line and is representative of configuration 6.

The wavelet analysis shows similar results for an undistorted flow as the method from Tryfonidis et al. [11]. On the one hand, however, there is the advantage of a better time resolution. Particularly, during the transition to rotating stall, signal changes can be identified more clearly. On the other hand, this is a single transducer analysis which can be applied in real engines with considerably less effort than is required for the circumferential array of transducers. The results obtained with this method were unsatisfactory with respect to the operation with distortion generators. Uhlmann [15] also introduced a 2-D wavelet analysis requiring only two transducers positioned circumferentially. These results, however, were only of partial significance.

VI. Conclusions

Detailed experimental investigations of coupled static and dynamic total pressure inlet distortions on the five-stage high-pressure compressor Rig212 were performed. The influence of distortions on the unsteady operating of the compressor and their interaction were analyzed. The use of Kulite pressure transducers was a focal point in the high-frequency data acquisition due to the fact that these transducers resist the strong mechanical and thermal operation loads generated by the distortion generators and the extreme flow conditions following the surge line.

The strongest impact of the total pressure distortions resulted from sector size variation. The variation of the compressor speed had a large impact because the altered compressor suction behavior causes a changed ram pressure at the distortion generators, thus directly affecting distortion intensity. The result was as expected: configurations 5 and 6 caused the largest loss of performance at maximum compressor speed.

The RDG speed also had a marked effect on the engine characteristics. Here, a slight increase of the compressor pressure ratio and a stronger increase of the reduced mass flow could be

observed for increasing distortion generator speed. When using the RDG alone, a decrease of the surge line was identified for characteristic speed ratios. In addition, a premature decrease occurred for corotating total pressure distortions. Peters [9] and Longley [2] assumed that these reductions are caused by the excitation of the relevant frequencies of modal waves and spikes as stall predecessors. In contrast, the coupled distortion generator operation seemed to have a dampening effect on the SDG, yielding a symmetric distortion distribution.

Because of static pressure gradients, the total pressure distortions in the compressor inlet are overlaid by vortical flow distortions. However, a dependence of vortical flow direction, that is, rotating direction of the RDG, on the global behavior of the compressor in the map could not be identified; merely a premature decrease of the surge line for corotating total pressure distortions was noted. This is in agreement with the results of Peters [9] and Longley [2]. No dependencies were identified in the unstable operating range.

The main results of the flow analysis of the compressor intake were the following. Stall is generated independent of compressor speed and configuration within a few rotor revolutions. A rapidly rotating spike develops into a full-span cell rotating in the annulus, the expansion and amplitude of this cell increasing with rising compressor speed. Surge is also initiated by the same process in Rig212.

The windowed Fourier transformation gave no indication of the imminent flow separation. Indeed, this method generated pseudo-frequencies that are not part of the signal. In the case of homogenous inflow, the circumferential analysis from Tryfonidis et al. [11] showed indications of rotating waves. The wavelet transformation, which yielded similar results in investigations using only one transducer, is more suitable for the resolution of high-frequency signal parts due to the dyadic division of the time frequency level. However, interpretation of the wavelet coefficients in the spectrogram is difficult because the plot lacks clarity owing to the lack of direct frequency data. For example, a periodicity in the signal cannot be interpreted as is the case for STFT; the wavelet transformation would require the individual investigation of the time-related occurrence of certain extreme points. We can see that the wavelet transformation has benefits that are not apparent at first glance. For instance, the Fourier transformation detects harmonic and low-frequency vibration parts with ease.

With regard to theoretical observations, the following is valid for evaluation of nonstationary pressure signals by means of the compressor tests. Low-frequency modal waves (long-length scale perturbations) in the signal can be detected more easily by means of the Fourier transformation. High-frequency spikes (short-length scale perturbations) can be detected more easily by means of the wavelet transformation, although (theoretical considerations) this cannot be confirmed by the results of the present investigations.

References

[1] Jahnen, W., "Untersuchung von Strömungsinstabilitäten in einem mehrstufigen Axialverdichter unter dem Einfluss von Eintrittsstörungen," Ph.D. Dissertation, Univ. der Bundeswehr Munich, Neubiberg, Germany, 1998.

[2] Longley, J. P., "Effects of Rotating Inlet Distortion on Multistage Compressor Stability," American Society of Mechanical Engineers Paper 94-GT-220, 1994.

[3] Scheidler, S. G., Mundt, Ch., Mettenleiter, M., Hermann, J., and Hiller, S. J., "Active Stability Control of the Compression System in a Twin-Spool Turbofan Engine by Air Injection," *The 10th International Symposium on Transport Phenomena and Dynamics of Rotating Machinery*, École Polytechnique Fédérale de Lausanne Paper 10-2004-73, 2004.

[4] Buhr, C. A., Franchek, M. A., and Fleeter, S., "Rotating Stall Control in Axial Compressors Subject to Wheel Speed Transients," *Journal of Propulsion and Power*, Vol. 22, No. 2, 2006, pp. 404–410. doi:10.2514/1.6272

[5] Reuß, N., "Untersuchung von kombinierten Eintrittstotaldruckstörungen auf das instationäre Betriebsverhalten eines fünfstufigen Hochdruckverdichters," Ph.D. Dissertation, Univ. der Bundeswehr Munich, Neubiberg, Germany, 2005.

[6] Moore, F. K., "Stall Transients of Axial Compression Systems with Inlet Distortion," *Journal of Propulsion and Power*, Vol. 2, No. 6, 1986, pp. 552–561. doi:10.2514/3.22941

[7] Fottner, L., "Strömungsmaschinen I und II Vorlesungsskript," Lecture Notes, Univ. der Bundeswehr Munich, Neubiberg, Germany, 2001.

[8] Roach, P. E., "The Generation of Nearly Isentropic Turbulence by Means of Grids," *Heat and Fluid Flow*, Vol. 8, No. 2, 1987, pp. 82–92. doi:10.1016/0142-727X(87)90001-4

[9] Peters, T., "Untersuchung von Strömungsinstabilitäten in einem mehrstufigen Axialverdichter unter dem Einfluss von rotierenden Eintrittsstörungen," Ph.D. Dissertation, Univ. der Bundeswehr Munich, Neubiberg, Germany, 2004.

[10] Day, I. J., and Freeman, C., "The Unstable Behaviour of Low and High Speed Compressors," American Society of Mechanical Engineers Paper 93-GT-26, 1993.

[11] Tryfonidis, M., Paduano, J. D., Hendricks, G., and Epstein, A. H., "Prestall Behavior of Several High Speed Compressors," *Journal of Turbomachinery*, Vol. 117, No. 1, Jan. 1995, pp. 62–80.

[12] Cumpsty, N. A., *Compressor Aerodynamics*, Univ. of Cambridge, Dept. of Engineering, Longman Scientific & Technical Group, Essex, England, UK, 1989.

[13] Greitzer, E. M., and Moore, F. K., "A Theory of Post-Stall Transients in Axial Compression Systems, Part I: Development of Equations," *Journal of Engineering for Gas Turbines and Power*, Vol. 106, Jan. 1986, pp. 68–76.

[14] Garnier, V. H., Epstein, A. H., and Greitzer, E. M., "Rotating Waves as a Stall Inception Indication in Axial Compressors," *Journal of Turbomachinery*, Vol. 113, No. 2, 1991, pp. 290–301. doi:10.1115/1.2929105

[15] Uhlmann, H. G., "Früherkennung aerodynamischer Verdichterinstabilitäten mittels Wavelet-Transformationsregeln," Ph.D. Dissertation, Technical Univ. of Munich, 2003.

[16] Brown, C., and Sawyer, S., "Wavelet Based Analysis of Rotating Stall and Surge in a High Speed Centrifugal Compressor," *38th AIAA/ASME/SAE/ASEE Joint Propulsion Conference and Exhibit*, AIAA Paper 2002-4080, 2002.

A. Prasad
Associate Editor